Ultrafast electron-lattice coupling dynamics in VO_2 and V_2O_3 thin films

Elsa Abreu,[1,*] Stephanie N. Gilbert Corder,[2] Sun Jin Yun,[3,4] Siming Wang,[5,6,7,8] Juan Gabriel Ramírez,[9] Kevin West,[10,5,6] Jingdi Zhang,[5,†] Salinporn Kittiwatanakul,[10] Ivan K. Schuller,[5,6,7] Jiwei Lu,[10] Stuart A. Wolf,[10,11] Hyun-Tak Kim,[3,4] Mengkun Liu,[2,‡] and Richard D. Averitt[5,§]

[1]*Institute for Quantum Electronics, Department of Physics, ETH Zurich, 8093 Zurich, Switzerland*
[2]*Department of Physics and Astronomy, Stony Brook University, Stony Brook, New York 11794, USA*
[3]*Metal-Insulator Transition Lab, ETRI, Daejeon 305-350, South Korea*
[4]*School of Advanced Device Technology, University of Science and Technology, Daejeon 305-333, South Korea*
[5]*Department of Physics, The University of California at San Diego, La Jolla, California 92093, USA*
[6]*Center for Advanced Nanoscience, The University of California at San Diego, La Jolla, California 92093, USA*
[7]*Materials Science and Engineering Program, The University of California at San Diego, La Jolla, California 92093, USA*
[8]*Materials Sciences Division, Lawrence Berkeley National Laboratory, Berkeley, California 94720, USA*
[9]*Department of Physics, Universidad de los Andes, Bogotá 111711, Colombia*
[10]*Department of Materials Science and Engineering, University of Virginia, Charlottesville, Virginia 22904, USA*
[11]*Department of Physics, University of Virginia, Charlottesville, Virginia 22904, USA*

(Received 19 January 2017; revised manuscript received 28 July 2017; published 21 September 2017)

Ultrafast optical pump–optical probe and optical pump–terahertz probe spectroscopy were performed on vanadium dioxide (VO_2) and vanadium sesquioxide (V_2O_3) thin films over a wide temperature range. A comparison of the experimental data from these two different techniques and two different vanadium oxides, in particular a comparison of the spectral weight oscillations generated by the photoinduced longitudinal acoustic modulation, reveals the strong electron-phonon coupling that exists in both materials. The low-energy Drude response of V_2O_3 appears more amenable than VO_2 to ultrafast strain control. Additionally, our results provide a measurement of the temperature dependence of the sound velocity in both systems, revealing a four- to fivefold increase in VO_2 and a three- to fivefold increase in V_2O_3 across the insulator-to-metal phase transition. Our data also confirm observations of strong damping and phonon anharmonicity in the metallic phase of VO_2, and suggest that a similar phenomenon might be at play in the metallic phase of V_2O_3. More generally, our simple table-top approach provides relevant and detailed information about dynamical lattice properties of vanadium oxides, paving the way to similar studies in other complex materials.

DOI: 10.1103/PhysRevB.96.094309

I. INTRODUCTION

Vanadium oxides are well-known examples of materials where the phases are determined by strong interactions between different degrees of freedom. Such complex systems, where charge, lattice, orbital, and spin contributions can be equally strong and are frequently coupled, exhibit a variety of phenomena including high-temperature superconductivity [1], colossal magnetoresistance [2], multiferroicity [3], and topological surface states [4]. Given the complex nature of these materials, the various phases are generally challenging to investigate experimentally. Ultrafast time-resolved techniques are a successful route to approach this problem [5,6]. In particular, time-resolved measurements in different energy ranges have contributed to the understanding of insulator-to-metal transitions (IMTs) in vanadium dioxide (VO_2) and vanadium sesquioxide (V_2O_3) as a function of temperature, pressure, and doping [7–15]. These measurements have also shed light on the nature of the different insulating phases in both systems [8,16–18] and on the electron-phonon coupling driven acoustic response in V_2O_3 [8,9].

Despite many ultrafast and static measurements, the exact mechanisms responsible for the IMTs in vanadium oxides and especially in VO_2 remain widely debated [19–27], namely, the contribution of electronic correlations (Mott-Hubbard picture) and of electron-lattice mediated effects (Peierls model) [17,23,28–30]. It is clear, however, that multiple pathways are possible to initiate pressure- and temperature-dependent transitions, and that electronic and lattice effects are strongly coupled [17,28,31,32]. Measurements that dynamically investigate this coupling are therefore essential to assist in understanding the nature of IMTs, which serves as the primary motivation for the present work.

Bulk VO_2 undergoes an IMT at 340 K, along with a monoclinic-to-rutile structural transition [19,33] (cf. phase diagram in Fig. S1a of the Supplemental Material [34]). In the low-temperature phase, the vanadium ions dimerize and tilt to form a nonmagnetic insulator [23]. Above-band-gap photoexcitation of the monoclinic insulator can promote electrons to antibonding states, causing repulsion between the dimerized vanadium ions and lattice expansion, followed by long-range shear rearrangements at the speed of sound [18,22].

*Previously at Department of Physics, Boston University, Boston, MA 02215, USA; elsabreu@phys.ethz.ch
†Previously at Department of Physics, Boston University, Boston, MA 02215, USA.
‡Previously at Department of Physics, Boston University, Boston, MA 02215, USA; mengkun.liu@stonybrook.edu
§Previously at Department of Physics, Boston University, Boston, MA 02215, USA; raveritt@physics.ucsd.edu

Above a critical fluence threshold, the metallic phase forms via nucleation and growth [17,30,35,36]. The acoustic and optical phonon landscape changes drastically across the IMT, and phonons have recently been seen to account for 2/3 of the entropy increase at the IMT and to stabilize the metallic phase [26,28]. These observations suggest that lattice effects play a significant role in driving the IMT in VO_2. Our experiments access the coupling between lattice and electronic properties, highlighting the important role played by the structure in determining the dynamic electronic response of VO_2.

V_2O_3 is a low-temperature monoclinic antiferromagnetic insulator which transitions to a paramagnetic rhombohedral metal above 155 K [19,37] (cf. phase diagram in Fig. S1b of the Supplemental Material [34]). Initial reports stated that the system exhibits a classical Mott-Hubbard transition where electrons localize to form the insulating phase [20,21]. However, more recent work points to electron-lattice effects contributing strongly to the first-order IMT in the undoped compound [24] and questions the equivalence of temperature and pressure routes in driving the phase transition in doped V_2O_3 [10]. The strong strain dependence of metallic V_2O_3 manifests via the large influence of ultrafast acoustic modulations on the spectral weight redistribution dynamics, particularly in the far-infrared region of the spectra corresponding to the low-energy Drude weight [9]. As with VO_2, our experimental results on V_2O_3 enhance the understanding of the role of the lattice in determining the electronic properties and dynamics, and, further, they enable a direct comparison between the two materials.

We therefore present a comparative ultrafast pump-probe study of photoinduced acoustic effects in VO_2 and V_2O_3, seen in both optical reflectivity and terahertz (THz) conductivity dynamics. Transient reflectivity measurements at 1.55 eV are sensitive to interband transitions in VO_2 and V_2O_3, with insulating gaps of 0.6 and 0.5 eV, respectively [23], while THz probes the quasiparticle dynamics, effectively yielding a dynamical measurement of the dc conductivity.

Our main conclusions are that (i) both VO_2 and V_2O_3 exhibit significant electron-phonon coupling, with V_2O_3 being significantly more amenable than VO_2 to Drude weight modulation; (ii) the acoustic signatures we observe appear to be quite robust against variations in crystallinity in the different thin-film samples under study; (iii) sound velocity increases by over a factor of three across the insulator-to-metal transition for both VO_2 and V_2O_3 thin films; and (iv) acoustic damping increases in both metallic phases, suggesting phonon entropy as a significant stabilization mechanism in both VO_2 and V_2O_3.

First, our results show that similar to V_2O_3 [8,9], VO_2 exhibits a modulation of the electronic response due to photoinduced acoustic effects, albeit to a lesser degree. This influence of small structural variations on the electronic behavior attests to significant electron-phonon coupling. In this case, electron-phonon coupling refers to the rate at which energy is transferred between electrons and phonon modes of the lattice as used in the two-temperature model [34,38], rather than to a strictly microscopic parameter. Second, thin-film samples with varying crystallinity exhibit different static and dynamic electronic responses. Variations in morphology and crystallinity are widely reported for thin-film samples of vanadium oxides due to, e.g., strain, mismatch with the substrate, and growth conditions. They translate into a significant density of defects in the system, mostly structural in nature but potentially including oxygen vacancies as well, which have a strong and distinct influence on the electronic response [32,36,39]. Thin films with fewer defects have properties closer to bulk and are therefore characterized by a larger THz conductivity in the metallic state and by larger photoinduced conductivity variations. Variations in the static metallic phase conductivity enable us to indirectly compare defect densities in the different thin films under study since a direct quantification of defects is extremely challenging to obtain. In contrast to the changes in the static electronic behavior, the dynamic acoustic signatures we observe appear to be quite robust against varying defect density in the thin films. Third, our data provide a temperature-dependent measure of the sound velocity in both VO_2 and V_2O_3 thin films, revealing an increase in the sound velocity across the insulator-to-metal transition, four- to fivefold for VO_2 and three- to fivefold for V_2O_3, i.e., significantly larger ($>2\times$) than reported previously in bulk single crystals [26,40]. Finally, we verify that acoustic damping increases in the metallic phase of VO_2 compared to the insulating phase, in agreement with previous reports that present phonon entropy as a stabilization mechanism for the metallic phase [28]. V_2O_3 exhibits a similarly increased damping in the metallic phase, hinting that phonon anharmonicity might also be much stronger than in the insulating phase, and that phonon effects might play a significant role in the IMT of this material as well.

II. EXPERIMENTAL METHODS

Transient optical reflectivity measurements were performed using 35 fs pulses at 800 nm (1.55 eV) from a 1 KHz repetition rate, 3 W average power Ti:sapphire regenerative amplifier. Pump and probe fluences were set at 1–4 mJ/cm^2 and $<10\ \mu$J/cm^2, respectively. THz pulses of 1 ps in duration were generated via optical rectification and detected by electro-optic sampling in ZnTe. In contrast to the optical measurements at 1.55 eV, the THz pulses (0.1–2.5 THz) effectively probe the low-energy Drude response [23], which is flat and devoid of any spectral features in the chosen frequency range. Transient optical reflectivity measurements at 800 nm, yielding $\Delta R/R$, and THz conductivity measurements [5], yielding $\Delta\sigma$, were performed in parallel, with the same pump conditions. In both cases, pump and probe beams were set at approximately normal incidence to the sample, with a pump focal spot size about ten times larger than that of the probe. The penetration depth of the 1.55 eV pulse is of the order of the sample thickness for the VO_2 and V_2O_3 thin-film samples used in this work (cf. Table SIII in the Supplemental Material [34]). Inhomogeneity in the excited volume is therefore not significant enough to affect the observed dynamics, meaning that both 800 nm and THz probe beams sample similarly excited regions.

Of particular relevance to this work is the ability to generate coherent acoustic phonons using ultrafast optical excitation. The ultrafast above-band-gap optical pulse is absorbed near the surface, causing a localized temperature increase. Thermal expansion leads to a transient stress which launches a strain

wave in the material. The propagating acoustic phonon modifies the frequency-dependent refractive index and can therefore be detected optically via modulation of $\Delta R/R$ at 800 nm, and of $\Delta\sigma$ around 1 THz. When the film thickness is of the order of the longitudinal acoustic phonon wavelength, an acoustic standing wave is generated and detected instead [41]. Analytic [42,43] and conceptual [41] aspects of the generation and detection of coherent acoustic modulations can be found in the literature [41–43].

Our samples consist of 75- and 50-nm-thick films of VO_2 on c-cut Al_2O_3 [44], 75-nm-thick films of V_2O_3 on c-cut Al_2O_3 [45], and 95-nm-thick films of V_2O_3 on r-cut Al_2O_3 [32]. The VO_2 films have a well-defined out-of-plane rutile c axis and three preferred in-plane orientations due to the hexagonal symmetry of the c-cut Al_2O_3 substrate [46]. The 75 nm V_2O_3 film has a well-defined rhombohedral out-of-plane [110] axis but is polycrystalline in plane, while the 95 nm film is nearly single crystalline throughout. No signatures of other vanadium oxides phases were detected in either of the samples beyond the nominal VO_2 or V_2O_3. All films are epitaxial and details of the fabrication can be found elsewhere [32,44,45]. Unless otherwise specified, the results presented in this paper correspond to the 75 nm films.

The sample temperature was set using a continuous-flow cryostat, pumped down to 10^{-6} mbar and equipped with a heating stage.

III. RESULTS

A. Temperature-dependent THz conductivity

Figure 1 shows the static THz conductivity of the 75 nm VO_2 and V_2O_3 films measured using THz spectroscopy. Figure 1(a) shows that the IMT in the VO_2 film occurs at $T_{IMT} = 360$ K, and that a maximum conductivity of 4800 $(\Omega\,\mathrm{cm})^{-1}$ is obtained at 380 K. V_2O_3 is seen from Fig. 1(b) to have $T_{IMT} = 160$ K, with a peak conductivity of 900 $(\Omega\,\mathrm{cm})^{-1}$ at 200 K. These measurements demonstrate that our VO_2 and V_2O_3 films behave similarly to bulk single crystals, which attests to the generality of our conclusions. Above 200 K, the V_2O_3 metallic state conductivity decreases dramatically (see Fig. S1 of the Supplemental Material [34]), beyond what would be expected from an increased electron-phonon scattering rate, due to the strongly correlated nature of this "bad" metal region [23,47]. The relative conductivity decrease in the VO_2 metallic state above 380 K is smaller compared to V_2O_3, with a 6% conductivity drop per 50 K for VO_2 and an 11% conductivity drop per 50 K for V_2O_3. This is consistent with suggestions that electronic correlations have a smaller impact on the metallic phase of VO_2 compared to metallic V_2O_3 [48,49], which enters a crossover region to a pure Mott-insulator phase above 450 K (see Fig. S1 of the Supplemental Material [34]). Corresponding temperature-dependent static conductivity data for the 95 nm V_2O_3 film are shown in Fig. S2 of the Supplemental Material [34].

B. Conductivity and reflectivity dynamics in VO_2

Figures 2(a), 3(a), and 3(b) show the transient conductivity ($\Delta\sigma$) and transient reflectivity at 800 nm ($\Delta R/R$) of VO_2 at low [Fig. 2(a)] and high [Figs. 3(a) and 3(b)] initial

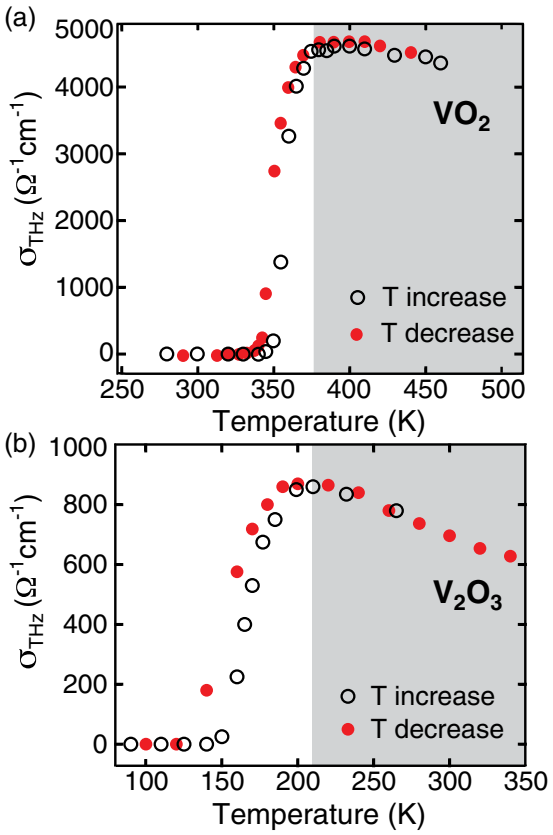

FIG. 1. Temperature dependence of the static far-infrared conductivity for the 75-nm-thick (a) VO_2 and (b) V_2O_3 thin films. Open black (solid red) symbols indicate increasing (decreasing) temperature. Both samples display hysteresis, characteristic of first-order phase transitions happening at 360 K in VO_2 and at 160 K in V_2O_3. The fully metallic region is shaded gray.

temperatures for a pump fluence of 3.8 mJ/cm^2. From the conductivity dynamics at $T < T_{IMT}$, shown in Fig. 2(a), it is clear that the maximum value achieved for the transient conductivity $\Delta\sigma(t)$ increases with initial temperature. Also, for $T = 77$ K, $\Delta\sigma(t)$ recovers in less than 10 ps, whereas for $T > 160$ K, the deposited energy is sufficient to thermally stabilize the metallic phase beyond our 350 ps measurement window [34]. As previously observed, the tens-of-ps time scale for the conductivity increase is considerably larger than the <1 ps electron-phonon thermalization time (see Fig. S7 of the Supplemental Material [34]) due to the nucleation and growth process that accompanies the IMT [35,50].

For $T > T_{IMT}$, the metallic phase dominates the transient photothermal response of VO_2. $\Delta\sigma$, shown in Fig. 3(a), decreases following photoexcitation, in agreement with Fig. 1(a), and so does $\Delta R/R$ [Fig. 3(b)]. Most significantly, the high-temperature dynamics of both $\Delta\sigma$ and $\Delta R/R$ exhibit oscillatory components [clearly isolated below, in Figs. 4(a) and 5(b)], which are direct signatures of acoustic wave propagation, similar to those reported in V_2O_3 [8,9]. Budai *et al.* [28] have observed that strongly anharmonic phonons rather than electronic effects stabilize the metallic phase of VO_2. The results shown here confirm the strength of electron-phonon coupling in metallic VO_2 since acoustic signatures are

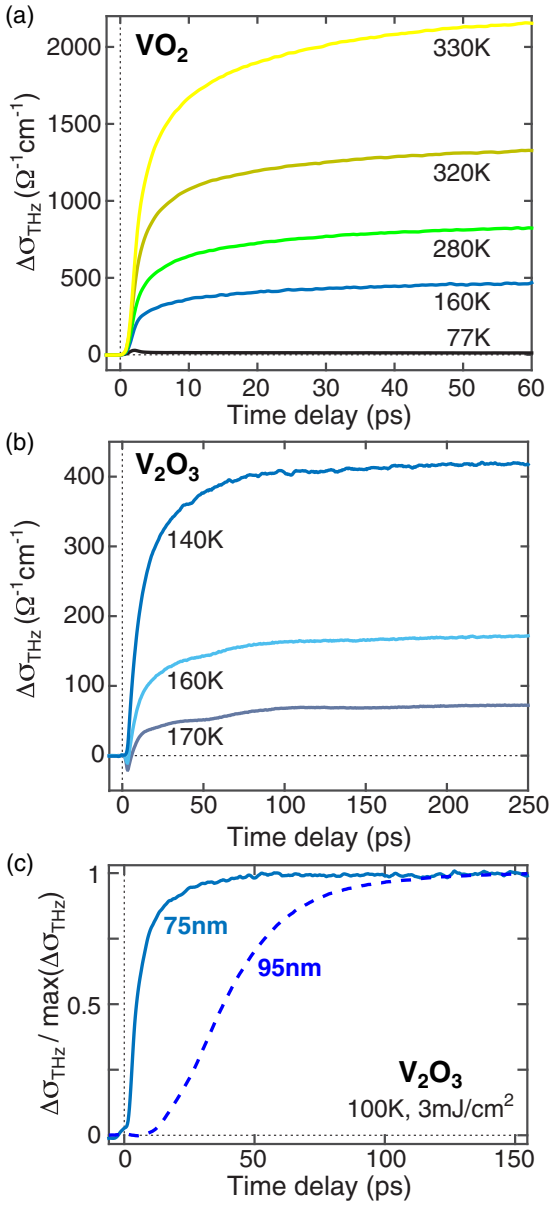

FIG. 2. Transient $\Delta\sigma$ of (a) 75-nm-thick VO_2, (b) 75-nm-thick V_2O_3, and (c) 75-nm- and 95-nm-thick V_2O_3 for temperatures below T_{IMT} at a pump fluence of (a) 3.8 mJ/cm^2, (b) 1 mJ/cm^2, and (c) 3 mJ/cm^2. Starting in the insulating phase, the THz response consists of a transient conductivity increase which corresponds to the IMT. (c) Comparison of the normalized $\Delta\sigma(t)$ for the 95 nm and 75 nm V_2O_3 films at 100 K, revealing a significant difference in IMT dynamics at short-time delays which arises from different defect densities in the films.

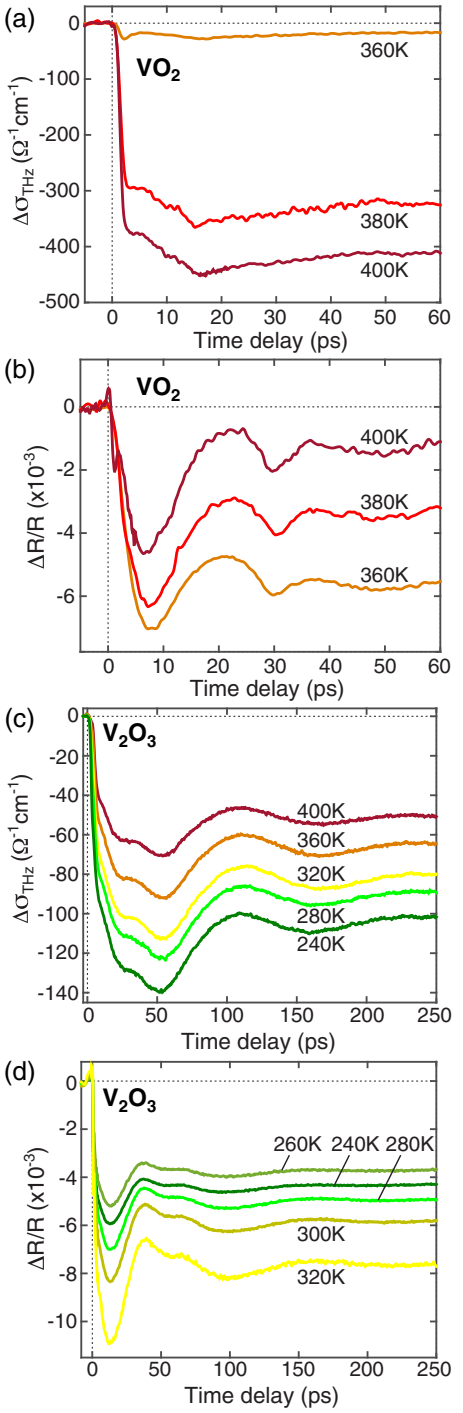

FIG. 3. Transient (a),(c) $\Delta\sigma$ and (b),(d) $\Delta R/R$ of 75-nm-thick (a),(b) VO_2 and (c),(d) V_2O_3 for temperatures above T_{IMT} at a pump fluence of (a),(b) 3.8 mJ/cm^2 and (c),(d) 1 mJ/cm^2. Shown are the metallic reflectivity responses, dominated by acoustic signatures, and the metallic conductivity responses, also with clear acoustic signatures.

seen not only in $\Delta R/R$, as expected, but also in $\Delta\sigma$, a clear indication that lattice dynamics modulate the Drude response of the system above T_{IMT}.

C. Conductivity and reflectivity dynamics in V_2O_3

As a counterpart to the data on VO_2, Figs. 2(b), 3(c), and 3(d) show $\Delta\sigma$ and $\Delta R/R$ for V_2O_3 at temperatures below [Fig. 2(b)] and above [Figs. 3(c) and 3(d)] T_{IMT} for a pump fluence of 1 mJ/cm^2. V_2O_3 also exhibits a tens-of-ps $\Delta\sigma$ increase characteristic of a percolative IMT [Fig. 2(b)]. The decrease in $\Delta\sigma$ with increasing initial temperature stems solely from the fact that temperatures closer to T_{IMT} are used compared to VO_2, so that the initial state already has a finite conductivity (Fig. 1) and the $\Delta\sigma$ response saturates as the full metallic state is reached. Photoexcitation of the system in

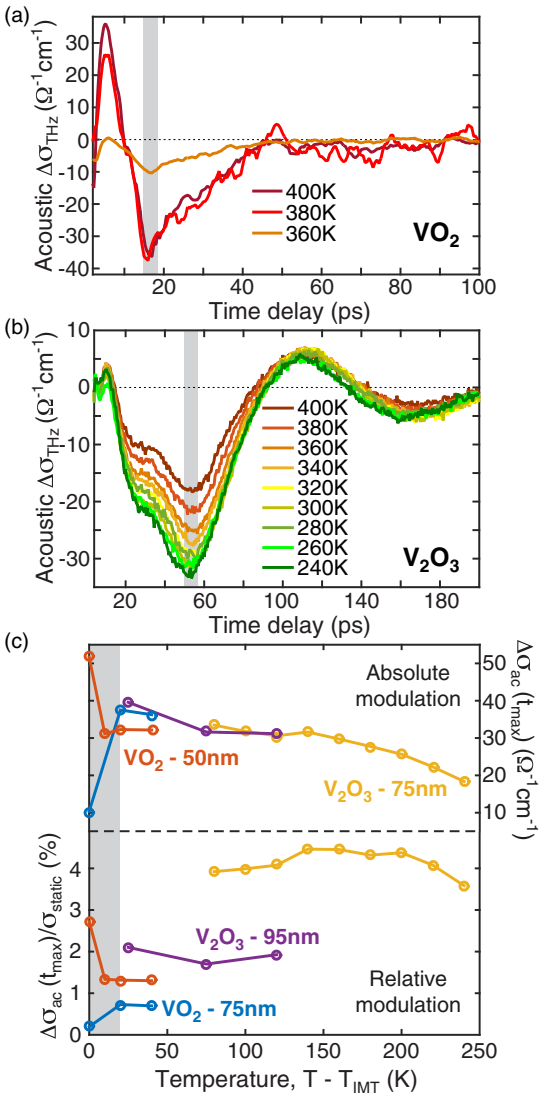

FIG. 4. Background-subtracted $\Delta\sigma$ acoustic oscillations for (a) VO_2 and (b) V_2O_3, corresponding to the data from Figs. 3(a) and 3(c). $\Delta\sigma(t)$ data for the VO_2 film were smoothed using a five-point (1 ps) moving average. Vertical gray bars indicate the time delays at which the values in (c) were calculated [34]. (c) Bottom: Temperature dependence of the maximum acoustic modulation of $\Delta\sigma$, normalized by the static conductivity at the corresponding temperature (see Fig. 1 and Fig. S2 of the Supplemental Material [34]). Top: Temperature dependence of the maximum acoustic modulation of $\Delta\sigma$. Data is shown for all four VO_2 and V_2O_3 films. A fluence of 3.8 mJ/cm^2 was used for the 75-nm-thick VO_2 film (blue), 4 mJ/cm^2 for the 50 nm VO_2 (orange), 1 mJ/cm^2 for the 75 nm V_2O_3 (yellow), and 3 mJ/cm^2 for the 95 nm V_2O_3 (purple). The gray shaded region corresponds to temperatures $T < T_{IMT} + 20$ K, where the influence of the IMT hysteresis could affect the results.

the metallic phase at $T > T_{IMT}$ produces a decrease of both $\Delta\sigma$ and $\Delta R/R$ in addition to clearly defined temperature-dependent acoustic signatures, as previously reported [8,9].

Figure 2(c) compares the normalized $\Delta\sigma(t)$ for the 95 nm and 75 nm V_2O_3 films at 100 K for a pump fluence of 3 mJ/cm^2. The 95 nm film has a metallic conductivity more than twice as large as the 75 nm film (see Fig. 1(b) and Fig. S2 of the Supplemental Material [34]), which is likely due to its single-crystalline rather than polycrystalline nature and to its consequent smaller defect density. As discussed in an earlier publication [50], the defect density has a strong influence not only on the static properties but also on the transition dynamics of V_2O_3 thin films, since it affects the nucleation and growth of metallic domains in the insulating phase. For V_2O_3 and VO_2, it is important to distinguish between ultrafast transition dynamics that occur at the microscopic level, independent of the nucleation and growth process, and those that occur at the mesoscopic level where the response is dominated by nucleation and growth. Microscopic effects have been extensively discussed, particularly in the case of VO_2 [23,35,51,52]. Using a THz probe, which is sensitive to the mesoscale dynamics, we observe fast $\Delta\sigma(t)$ transients that start during photoexcitation by the pump pulse for the 75 nm film, whereas the 95 nm film exhibits slower variations and a delayed onset relative to the pump arrival time [Fig. 2(c)]. These significant differences in conductivity dynamics cannot be explained by the minimal difference in film thickness. Rather, they occur due to the 95 nm film containing fewer defects than the 75 nm film, and hence fewer defect-induced preferential nucleation sites, which slows down the photoinduced IMT in the thicker sample [50]. Such mesoscopic effects occur independently in addition to any microscopic modifications, and their effect on the dynamics must be taken into account in studies of both V_2O_3 and VO_2.

D. Acoustic dynamics—dependence on film thickness and temperature

Despite differences in IMT time scales (see Fig. 2(c) and Fig. S5 of the Supplemental Material [34]), high-temperature dynamic data for the 50 nm VO_2 film and the 95 nm V_2O_3 film are comparable to the 75 nm films of each material and, consequently, are shown in Fig. S4 of the Supplemental Material [34].

Finally, $\Delta R/R$ dynamics for VO_2 and V_2O_3 at $T < T_{IMT}$ also exhibit acoustic oscillations that are characteristic of the insulating phase. The full $\Delta R/R$ dynamic insulating responses have many contributing factors and are therefore less straightforward to analyze than the metallic responses. As the present work focuses on the acoustic component, the full low-temperature $\Delta R/R$ signals are shown in Fig. S3 of the Supplemental Material [34]. The acoustic signatures of the insulating phase can, however, be compared with the metallic phase results of Figs. 3(b) and 3(d), as shown in Fig. 5 and discussed in Sec. IV below.

IV. ANALYSIS AND DISCUSSION

In order to analyze the acoustic dynamics in more detail, we subtract all exponential nonoscillatory contributions to the metallic data in Fig. 3, as detailed in the Supplemental Material [34]. These exponential components of the dynamics, caused by nonlinear electronic responses and by thermal decay, are consistent with previously reported measurements [7–9,13,15,16,53], but their detailed discussion is beyond the scope of our present work. Background subtraction yields the acoustic contribution to $\Delta\sigma(t)$, shown in Fig. 4, and to

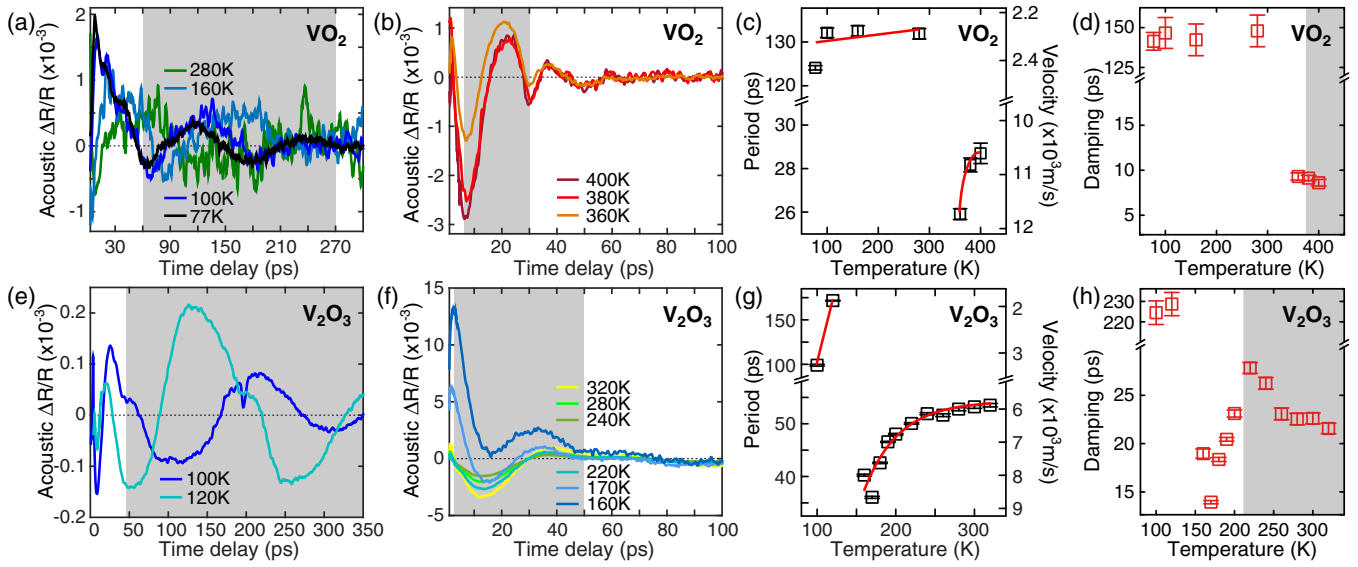

FIG. 5. Background-subtracted $\Delta R/R$ acoustic oscillations for (a) insulating and (b) metallic VO_2 and for (e) insulating and (f) metallic V_2O_3, corresponding to the data in Figs. 3(b), 3(d), and also Fig. S3 of the Supplemental Material [34]. Plots to the right show the temperature dependence of (c),(g) the acoustic oscillation period and the corresponding sound velocity, as well as of (d),(h) the damping time, for (c),(d) VO_2 and for (g),(h) V_2O_3, extracted by fitting the shaded regions of (a), (b), (e), and (f) with a damped sinusoid. Red lines in (c) and (g) are linear fits [(c),(g): insulating phase], an exponential guide to the eye [(c): metallic phase], and an exponential fit [(g): metallic phase]. In (d) and (h), the fully metallic region is shaded gray, for comparison with Fig. 1.

the $\Delta R/R$ dynamics, shown in Fig. 5. The lack of acoustic signatures in the insulating phase $\Delta\sigma(t)$ response in Figs. 2(a) and 2(b) is expected since the THz probe is only sensitive to the metallic volume fraction [50].

A. Transient acoustic modulation of the THz conductivity

The acoustic component of the $\Delta\sigma$ dynamics is shown in Figs. 4(a) and 4(b) for VO_2 and V_2O_3, respectively. The modulation is significantly longer lived in V_2O_3, an indication that phonon damping is smaller in V_2O_3 than in VO_2. The significance of phonon damping for the properties of VO_2 and V_2O_3 will be discussed in more detail below.

In Fig. 4(c), the maximum $\Delta\sigma$ oscillation amplitude for both VO_2 and V_2O_3 is plotted as a function of $T - T_{IMT}$. The maximum is estimated at the time delays marked by vertical gray bars in Figs. 4(a) and 4(b) to avoid potential residual contributions from nonacoustic effects at shorter time delays. The choice of temperature scale enables a direct comparison between the different samples and materials. The bottom part of Fig. 4(c) shows the oscillation amplitude maxima normalized by the static conductivity at that temperature [34], while the top shows the non-normalized values. For $T > T_{IMT} + 20$ K, i.e., well outside the hysteresis region (Fig. 1), the absolute value of the maximum conductivity modulation [top of Fig. 4(c)] decreases with increasing temperature for all films. This decrease is consistent with the negative slope of the static conductivity observed with increasing temperature in the metallic phase (see Fig. 1 and Fig. S2 of the Supplemental Material [34]). Interestingly, the conductivity oscillation amplitudes are very similar for all the samples examined, even after accounting for the differences in pump fluence (the fluence dependence for the two V_2O_3 samples is discussed in Sec. II F and Fig. S6 of the Supplemental Material [34]). In particular, oscillation amplitudes are comparable for VO_2 and V_2O_3, as well as for samples of the same material with different static conductivities.

The normalized plot in Fig. 4(c) (bottom) enables a more direct comparison of VO_2 and V_2O_3 results since it provides a measure of the effective acoustic modulation, independent of the overall conductivity of the sample. It is clear that acoustic modulations in the 75-nm-thick V_2O_3 are stronger than in VO_2, which points to larger electron-phonon-induced strain modulation. This conclusion is further strengthened if the different pump fluences are taken into account when analyzing the data (cf. Sec. II F and Fig. S6 of the Supplemental Material [34]). The 95-nm-thick V_2O_3 film does not show such a strikingly higher effect compared to VO_2. This could be due to lower acoustic impedance between sample and substrate in this 95 nm V_2O_3 film, the only single-crystalline system among all epitaxial films under study, which would cause a decrease in the amplitude of acoustic modulations. The normalized plot of Fig. 4(c) also shows that the effective acoustic modulation displays no clear dependence on temperature.

B. Acoustic modulation of $\Delta R/R$—temperature dependence of the sound velocity

It is not trivial to relate the acoustic oscillation period in $\Delta\sigma(t)$ with the sound velocity in the system since the THz probe, with its $\sim$300 μm wavelength, effectively probes an average acoustic modulation of the conductivity in the submicron-thick films [9]. However, an approximate sound velocity value can be directly determined using oscillations of $\Delta R/R$, the transient reflectivity at 800 nm [42]. A model of the $\Delta R/R$ response expected for a strain-modulated thin film following photoexcitation is given in Sec. III and Fig. S7 of the Supplemental Material [34]. The success of this model

in reproducing the data on a thicker V_2O_3 film serves as a validation of the use of $\Delta R/R$ oscillations to extract sound velocity values.

We focus on the acoustic oscillations which are isolated in Fig. 5, obtained from the data in Figs. 3(b) and 3(d) for $T > T_{IMT}$, and in Fig. S3 of the Supplemental Material [34] for $T < T_{IMT}$. Acoustic modulations of $\Delta R/R$ for $T < T_{IMT}$ are more difficult to observe in V_2O_3 than in VO_2 as the current measurements are limited to temperatures above 80 K. Indeed, the lower value of T_{IMT} for V_2O_3 compared to VO_2, as well as the fact that the latent heat is smaller and therefore the IMT can be driven at the same fluence for lower temperatures relative to T_{IMT}, means that the acoustic response of the insulating phase in V_2O_3 is quickly masked by phase transition dynamics. This problem could be circumvented in future work by analyzing the response at lower temperatures or by studying doped V_2O_3 samples.

The period of the reflectivity oscillations shown in Figs. 5(c) and 5(g) is determined by fitting the shaded regions in the corresponding reflectivity data with a damped sinusoid, $\Delta R = \Delta R_0 + A\exp(-t/t_d)\sin[2\pi(t-t_0)/\tau]$, where τ is the period and t_d is the damping time. The fidelity of the fit is validated by the near unity adjusted R^2 values (cf. Sec. II D of the Supplemental Material [34]). Given that the 75 nm thickness of the films is of the order of acoustic phonon wavelengths [40], the observed oscillations are essentially reflections of the acoustic wave between the film surface and the film-substrate interface, as described in Sec. I. The corresponding sound velocity can therefore be calculated from the period τ using $v_{sound} = 4d/\tau$ [41,42], where d is the film thickness.

The most striking effect in these data is that the sound velocity associated with these oscillations, apart from a slow and monotonic increase with temperature, exhibits an abrupt increase at T_{IMT} when going from the insulating to the metallic phase, by a factor of 4–5 in VO_2 and 3–5 in V_2O_3. This is seen clearly in Figs. 5(c) and 5(g). Such a large sound velocity variation is not unexpected in vanadium oxides, where lattice constants change by about 1% across the structural phase transition that accompanies the IMT [34,37,54]. V-O and V-V bond lengths change by up to 4% across the structural transition, on average, stabilizing an insulating phase below T_{IMT} or a metallic phase above T_{IMT} [33,34,55].

Previous sound velocity measurements for the metallic phase of VO_2 bulk single crystals yield approximately 4×10^3 m/s, measured along the rutile c axis for surface Rayleigh waves by Maurer *et al.* [26], or 8×10^3 m/s, determined from the phonon dispersion of the longitudinal acoustic mode along the Γ-Z direction in Budai *et al.* [28]. In the metallic phase of V_2O_3, Seikh *et al.* [40] and Yelon *et al.* [56] report 8×10^3 m/s, corresponding to longitudinal acoustic mode propagation. The VO_2 and V_2O_3 metallic sound velocities shown in Fig. 5 are consistent with the order of magnitude reported previously. Maurer *et al.* [26] and Seikh *et al.* [40] also measure the sound velocity across the IMT, for VO_2 and V_2O_3, respectively, and find variations by a factor of at most 1.5, which is smaller than the one we report in this work. We note, however, that these previous measurements were performed on bulk samples, while our current results correspond to thin-film properties. Some difference in the absolute value of the sound velocity as well as in its variation across the IMT is expected between bulk and thin-film samples, as discussed below. Our work quantifies this difference using a method which can easily be extended to other systems.

Sample-to-sample variation in vanadium oxides, and in particular in vanadium oxide thin films, is well known and must be taken into account when analyzing and comparing different data sets [39]. In particular, variation in sound velocity values is a result of the different strain environments and crystallinity of the samples. The strain sensitivity of VO_2 material properties, in particular, is widely reported [39,57–60] and is caused by large differences in lattice constant values along different crystallographic axes with large variations of these values across the IMT (see Table SI of the Supplemental Material [34]). For the measurements presented here, sound velocity determination could be affected by acoustic waves propagating at an angle to the film normal, by substrate-induced strain in the growth direction as well as by contributions from other acoustic modes in the system, in particular nonlongitudinal waves.

C. Increased phonon damping in the metallic phase

Analyzing Figs. 4(a) and 4(b) and Figs. 5(b) and 5(f) from the perspective of acoustic modulation damping reveals that the amplitude of the metallic phase $\Delta\sigma$ and $\Delta R/R$ oscillations decays faster in VO_2 than in V_2O_3. The damped sinusoid fit to the metallic $\Delta R/R$ data yields damping times of about 10 ps for VO_2 [Fig. 5(d)] and 20 ps for V_2O_3 [Fig. 5(h)] (see also Supplemental Material [34]). Damping effects are thus stronger in the metallic phase of VO_2 compared to V_2O_3. The observations from Budai *et al.* [28] of increased phonon damping in the metallic phase compared to the insulating phase are verified by our analysis on VO_2, where the damping time decreases from 145 ps in the insulator to 10 ps in the metal. The results for V_2O_3 show a decrease in damping time from 225 ps in the insulating phase to 20 ps in the metallic phase, suggesting a similar influence of phonon anharmonicity to be at play in the metallic phase of V_2O_3. It should be noted that an additional source of damping exists, due to transmission of the acoustic wave into the substrate. Transmission losses will depend on how well acoustic impedances are matched between the film and the substrate, and can potentially lead to an increased effective damping time associated with the VO_2 or V_2O_3 material responses alone. Quantitative comparisons with damping times obtained from other methods must therefore be done with care. Details of the damping analysis are presented in Sec. II D of the Supplemental Material [34].

D. Discussion

Figures 4 and 5 provide a measure of photoinduced acoustic signatures in VO_2 and V_2O_3. It is interesting to compare the temperature dependence of the different properties of the system. While the static conductivity, sound velocity, and acoustic damping all vary with temperature in the metallic phase, the effective acoustic modulation [normalized plot at the bottom of Fig. 4(c)] shows no clear temperature dependence.

Comparing VO_2 and V_2O_3 in Figs. 4 and 5 enables us to conclude that acoustic signatures are qualitatively the same

and quantitatively within a factor of two of each other. This is so despite differences in the mechanism that drives the IMT, in particular the larger effect expected from electronic correlations in V_2O_3 compared to VO_2, and in the latent heat associated with the IMT (65 J/cm^3 for V_2O_3 [61] and 240 J/cm^3 for VO_2 [62]). In the remainder of the paper, we discuss the possible origin of the larger acoustic modulation signal that is observed for V_2O_3. First, the electron-phonon coupling coefficient is higher for V_2O_3 (3×10^{18} W K^{-1} m^{-3} [34]) than for VO_2 (10^{18} W K^{-1} m^{-3} [63]), which partially explains the increased signal strength since energy couples more efficiently between the electrons and the lattice. This means that the strain wave generation process following electronic photoexcitation is more efficient in V_2O_3, and that the subsequent strain-induced modifications of the electronic spectral weight are stronger. In fact, metallic V_2O_3 at atmospheric conditions is seen to lie near a transition line to a pressure-induced isostructural paramagnetic insulating phase (see Fig. S1 of the Supplemental Material [34]), so that one would indeed expect a similar pressure change to lead to a larger change in the conductivity for V_2O_3 than for VO_2. Second, the lattice structure of V_2O_3 is overall more amenable to modulations, as deduced from the lower phonon damping measured in V_2O_3 compared to VO_2, which effectively means that the structure is less rigid. This implies that photoinduced strain modulations would be larger in V_2O_3 for the same amount of energy transferred to the lattice. Lastly, it is important to reiterate the strong influence of differences in defect density, which lead to variations in the static and dynamic properties of both VO_2 and V_2O_3 when comparing nominally equivalent samples. In particular, such variations are known to affect the structural response of these materials [32] and should therefore be taken into account when attempting precise quantitative comparisons.

V. CONCLUSION

This work demonstrates that strong electron-phonon coupling exists and is responsible for clear ultrafast acoustic modulations of the Drude and optical responses in V_2O_3 and VO_2. This effect appears to be stronger for V_2O_3 than for VO_2, suggesting that the electronic and lattice structures of V_2O_3 are more amenable to transient strain modulation than those of VO_2.

We further identify a significant temperature dependence of the sound velocity in both materials, in particular a dramatic increase by a factor of 4–5 in VO_2 and 3–5 in V_2O_3 across the IMT. The observation (in both materials) of stronger acoustic damping in the metallic phase relative to the insulating one confirms the strong role of phonon anharmonicity in metallic VO_2 and suggests that a similar mechanism is at play in V_2O_3. The time scale for damping of the acoustic modulations in both the THz conductivity (Drude response) and the near-infrared reflectivity (spectral weight at 1.55 eV, related to the occupation of V3*d* orbitals) are longer for V_2O_3 than for VO_2, indicating stronger damping in the latter and thus a potentially stronger phonon anharmonicity contribution.

Our findings demonstrate that transient strain induced by photoexcitation is a useful tool to both analyze and control the electronic properties of complex materials and their coupling to lattice excitations. The same approach could be used to investigate the modifications to the electronic and lattice properties induced by different defect densities. This is particularly relevant in the case of VO_2 and V_2O_3, where different defect densities lead to strong sample-to-sample variation of static and dynamic properties, but is likely applicable to other complex materials and to their properties which are characteristically sensitive to small perturbations.

ACKNOWLEDGMENTS

We thank Mariano Trigo and Gabriel Lantz for useful discussions. E.A. acknowledges support from the ETH Zurich Postdoctoral Fellowship Program and from the Marie Curie Actions for People COFUND Program. R.D.A. and E.A. acknowledge support from the US Department of Energy, Basic Energy Sciences, under Grant No. DE-FG02-09ER46643. S.J.Y. and H.-T.K. acknowledge support from the MIT project at ETRI. S.J.Y. acknowledges support from project (MSIT, 2016-0-00576). I.K.S., S.W., J.G.R., and K.W. acknowledge support from AFOSR under Grant No. FA9550-16-1-0026. I.K.S. acknowledges support from the Vannevar Bush Faculty Fellowship program sponsored by the Basic Research Office of the Assistant Secretary of Defense for Research and Engineering and funded by the Office of Naval Research through Grant No. N00014-15-1-2848. J.G.R. kindly acknowledges support from the FAPA program through Facultad de Ciencias and Vicerrectoria de Investigaciones of Universidad de los Andes, Bogotá, Colombia, and Colciencias Grant No. 120471250659.

E.A. and S.N.G.C. contributed equally to this work.

[1] M. Hashimoto, E. A. Nowadnick, R.-H. He, I. M. Vishik, B. Moritz, Y. He, K. Tanaka, R. G. Moore, D. Lu, Y. Yoshida, M. Ishikado, T. Sasagawa, K. Fujita, S. Ishida, S. Uchida, H. Eisaki, Z. Hussain, T. P. Devereaux, and Z.-X. Shen, Nat. Mater. **14**, 37 (2014).

[2] S. Jin, T. H. Tiefel, M. McCormack, R. A. Fastnacht, R. Ramesh, and L. H. Chen, Science **264**, 413 (1994).

[3] T. Kubacka, J. A. Johnson, M. C. Hoffmann, C. Vicario, S. de Jong, P. Beaud, S. Grübel, S.-W. Huang, L. Huber, L. Patthey, Y.-D. Chuang, J. J. Turner, G. L. Dakovski, W.-S. Lee, M. P. Minitti, W. Schlotter, R. G. Moore, C. P. Hauri, S. M. Koohpayeh, V. Scagnoli, G. Ingold, S. L. Johnson, and U. Staub, Science **343**, 1333 (2014).

[4] Y. H. Wang, H. Steinberg, P. Jarillo-Herrero, and N. Gedik, Science **342**, 453 (2013).

[5] R. D. Averitt and A. J. Taylor, J. Phys.: Condens. Matter **14**, R1357 (2002).

[6] J. Orenstein, Phys. Today **65**(9), 44 (2012).

[7] O. V. Misochko, M. Tani, K. Sakai, K. Kisoda, S. Nakashima, V. N. Andreev, and F. A. Chudnovsky, Phys. Rev. B **58**, 12789 (1998).

[8] B. Mansart, D. Boschetto, S. Sauvage, A. Rousse, and M. Marsi, Europhys. Lett. **92**, 37007 (2010).

[9] M. K. Liu, B. Pardo, J. Zhang, M. M. Qazilbash, S. J. Yun, Z. Fei, J.-H. Shin, H.-T. Kim, D. N. Basov, and R. D. Averitt, Phys. Rev. Lett. **107**, 066403 (2011).

[10] F. Rodolakis, P. Hansmann, J. P. Rueff, A. Toschi, M. W. Haverkort, G. Sangiovanni, A. Tanaka, T. Saha-Dasgupta, O. K. Andersen, K. Held, M. Sikora, I. Alliot, J. P. Itié, F. Baudelet, P. Wzietek, P. Metcalf, and M. Marsi, Phys. Rev. Lett. **104**, 047401 (2010).

[11] A. Cavalleri, C. Tóth, C. W. Siders, J. A. Squier, F. Ráksi, P. Forget, and J. C. Kieffer, Phys. Rev. Lett. **87**, 237401 (2001).

[12] M. A. Huber, M. Plankl, M. Eisele, R. E. Marvel, F. Sandner, T. Korn, C. Schüller, J. R. F. Haglund, R. Huber, and T. L. Cocker, Nano Lett. **16**, 1421 (2016).

[13] B. T. O'Callahan, A. C. Jones, J. Hyung Park, D. H. Cobden, J. M. Atkin, and M. B. Raschke, Nat. Commun. **6**, 6849 (2015).

[14] G. Lantz, B. Mansart, D. Grieger, D. Boschetto, N. Nilforoushan, E. Papalazarou, N. Moisan, L. Perfetti, V. L. R. Jacques, D. L. Bolloc'h, C. Laulhé, S. Ravy, J. P. Rueff, T. E. Glover, M. P. Hertlein, Z. Hussain, S. Song, M. Chollet, M. Fabrizio, and M. Marsi, Nat. Commun. **8**, 13917 (2017).

[15] S. Wang, J. G. Ramírez, J. Jeffet, S. Bar-Ad, D. Huppert, and I. K. Schuller, Europhys. Lett. **118**, 27005 (2017).

[16] A. Pashkin, C. Kübler, H. Ehrke, R. Lopez, A. Halabica, R. F. Haglund, R. Huber, and A. Leitenstorfer, Phys. Rev. B **83**, 195120 (2011).

[17] D. Wegkamp, M. Herzog, L. Xian, M. Gatti, P. Cudazzo, C. L. McGahan, R. E. Marvel, R. F. Haglund, A. Rubio, M. Wolf, and J. Stähler, Phys. Rev. Lett. **113**, 216401 (2014).

[18] A. X. Gray *et al.*, arXiv:1601.07490.

[19] F. J. Morin, Phys. Rev. Lett. **3**, 34 (1959).

[20] D. B. McWhan, T. Rice, and J. P. Remeika, Phys. Rev. Lett. **23**, 1384 (1969).

[21] D. B. McWhan, J. P. Remeika, T. M. Rice, W. F. Brinkman, J. P. Maita, and A. Menth, Phys. Rev. Lett. **27**, 941 (1971).

[22] P. Baum, D.-S. Yang, and A. H. Zewail, Science **318**, 788 (2007).

[23] M. M. Qazilbash, A. A. Schafgans, K. S. Burch, S. J. Yun, B. G. Chae, B. J. Kim, H.-T. Kim, and D. N. Basov, Phys. Rev. B **77**, 115121 (2008).

[24] P. Pfalzer, G. Obermeier, M. Klemm, S. Horn, and M. L. denBoer, Phys. Rev. B **73**, 144106 (2006).

[25] P. Limelette, A. Georges, D. Jérome, P. Wzietek, P. Metcalf, and J. M. Honig, Science **302**, 89 (2003).

[26] D. Maurer, A. Leue, R. Heichele, and V. Müller, Phys. Rev. B **60**, 13249 (1999).

[27] L. Baldassarre, A. Perucchi, D. Nicoletti, A. Toschi, G. Sangiovanni, K. Held, M. Capone, M. Ortolani, L. Malavasi, M. Marsi, P. Metcalf, P. Postorino, and S. Lupi, Phys. Rev. B **77**, 113107 (2008).

[28] J. D. Budai, J. Hong, M. E. Manley, E. D. Specht, C. W. Li, J. Z. Tischler, D. L. Abernathy, A. H. Said, B. M. Leu, L. A. Boatner, R. J. Mcqueeney, and O. Delaire, Nature (London) **515**, 535 (2014).

[29] Z. Tao, Tzong-Ru T. Han, S. D. Mahanti, P. M. Duxbury, F. Yuan, C.-Y. Ruan, K. Wang, and J. Wu, Phys. Rev. Lett. **109**, 166406 (2012).

[30] V. R. Morrison, R. P. Chatelain, K. L. Tiwari, A. Hendaoui, A. Bruhács, M. Chaker, and B. J. Siwick, Science **346**, 445 (2014).

[31] A. X. Gray, J. Jeong, N. P. Aetukuri, P. Granitzka, Z. Chen, R. Kukreja, D. Higley, T. Chase, A. H. Reid, H. Ohldag, M. A. Marcus, A. Scholl, A. T. Young, A. Doran, C. A. Jenkins, P. Shafer, E. Arenholz, M. G. Samant, S. S. P. Parkin, and H. A. Dürr, Phys. Rev. Lett. **116**, 116403 (2016).

[32] J. G. Ramírez, T. Saerbeck, S. Wang, J. Trastoy, M. Malnou, J. Lesueur, J.-P. Crocombette, J. E. Villegas, and I. K. Schuller, Phys. Rev. B **91**, 205123 (2015).

[33] M. Marezio, D. B. McWhan, J. P. Remeika, and P. D. Dernier, Phys. Rev. B **5**, 2541 (1972).

[34] See Supplemental Material at http://link.aps.org/supplemental/10.1103/PhysRevB.96.094309 for (i) a summary of material properties, (ii) raw data and technical analysis details, and (iii) complementary data.

[35] D. J. Hilton, R. P. Prasankumar, S. Fourmaux, A. Cavalleri, D. Brassard, M. A. El Khakani, J. C. Kieffer, A. J. Taylor, and R. D. Averitt, Phys. Rev. Lett. **99**, 226401 (2007).

[36] S. Lysenko, V. Vikhnin, A. Rúa, F. Fernández, and H. Liu, Phys. Rev. B **82**, 205425 (2010).

[37] D. B. McWhan and J. P. Remeika, Phys. Rev. B **2**, 3734 (1970).

[38] P. B. Allen, Phys. Rev. Lett. **59**, 1460 (1987).

[39] M. Liu, A. J. Sternbach, M. Wagner, T. V. Slusar, T. Kong, S. L. Bud'ko, S. Kittiwatanakul, M. M. Qazilbash, A. McLeod, Z. Fei, E. Abreu, J. Zhang, M. Goldflam, S. Dai, G.-X. Ni, J. Lu, H. A. Bechtel, M. C. Martin, M. B. Raschke, R. D. Averitt, S. A. Wolf, H.-T. Kim, P. C. Canfield, and D. N. Basov, Phys. Rev. B **91**, 245155 (2015).

[40] M. M. Seikh, C. Narayana, A. K. Sood, P. Murugavel, M. W. Kim, P. A. Metcalf, J. M. Honig, and C. N. R. Rao, Solid State Commun. **138**, 466 (2006).

[41] S. Ge, X. Liu, X. Qiao, Q. Wang, Z. Xu, J. Qiu, P.-H. Tan, J. Zhao, and D. Sun, Sci. Rep. **4**, 5722 (2014).

[42] C. Thomsen, J. Strait, Z. Vardeny, H. J. Maris, J. Tauc, and J. J. Hauser, Phys. Rev. Lett. **53**, 989 (1984).

[43] C. Thomsen, H. T. Grahn, H. J. Maris, and J. Tauc, Phys. Rev. B **34**, 4129 (1986).

[44] K. G. West, J. Lu, J. Yu, D. Kirkwood, W. Chen, Y. Pei, J. Claassen, and S. A. Wolf, J. Vac. Sci. Technol. A **26**, 133 (2008).

[45] S. J. Yun, J. W. Lim, J.-S. Noh, B.-J. Kim, and H.-T. Kim, Jpn. J. Appl. Phys. **48**, 04C139 (2009).

[46] S. Kittiwatanakul, Ph.D. thesis, University of Virginia, 2014, sect. 2.3.2.

[47] M. M. Qazilbash, K. S. Burch, D. Whisler, D. Shrekenhamer, B. G. Chae, H.-T. Kim, and D. N. Basov, Phys. Rev. B **74**, 205118 (2006).

[48] D. N. Basov, R. D. Averitt, D. Van Der Marel, M. Dressel, and K. Haule, Rev. Mod. Phys. **83**, 471 (2011).

[49] M. K. Stewart, D. Brownstead, S. Wang, K. G. West, J. G. Ramírez, M. M. Qazilbash, N. B. Perkins, I. K. Schuller, and D. N. Basov, Phys. Rev. B **85**, 205113 (2012).

[50] E. Abreu, S. Wang, J. G. Ramírez, M. Liu, J. Zhang, K. Geng, I. K. Schuller, and R. D. Averitt, Phys. Rev. B **92**, 085130 (2015).

[51] M. K. Liu, M. Wagner, E. Abreu, S. Kittiwatanakul, A. McLeod, Z. Fei, M. Goldflam, S. Dai, M. M. Fogler, J. Lu, S. A. Wolf, R. D. Averitt, and D. N. Basov, Phys. Rev. Lett. **111**, 096602 (2013).

[52] S. A. Dönges, O. Khatib, B. T. O'Callahan, J. M. Atkin, J. H. Park, D. Cobden, and M. B. Raschke, Nano Lett. **16**, 3029 (2016).

[53] A. Cavalleri, T. Dekorsy, H. H. W. Chong, J. C. Kieffer, and R. W. Schoenlein, Phys. Rev. B **70**, 161102(R) (2004).
[54] D. Kucharczyk and T. Niklewski, J. Appl. Crystallogr. **12**, 370 (1979).
[55] P. D. Dernier and M. Marezio, Phys. Rev. B **2**, 3771 (1970).
[56] W. B. Yelon and J. E. Keem, Solid State Commun. **29**, 775 (1979).
[57] J. B. Goodenough, J. Solid State Chem. **3**, 490 (1971).
[58] J. Wu, Q. Gu, B. S. Guiton, N. P. D. Leon, L. Ouyang, and H. Park, Nano Lett. **6**, 2313 (2006).
[59] J. H. Park, J. M. Coy, T. S. Kasirga, C. Huang, Z. Fei, S. Hunter, and D. H. Cobden, Nature (London) **500**, 431 (2013).
[60] S. Kittiwatanakul, S. A. Wolf, and J. Lu, Appl. Phys. Lett. **105**, 073112 (2014).
[61] H. Keer, D. Dickerson, H. Kuwamoto, H. Barros, and J. Honig, J. Solid State Chem. **19**, 95 (1976).
[62] G. Chandrashekhar, H. Barros, and J. Honig, Mater. Res. Bull. **8**, 369 (1973).
[63] M. Liu, H. Y. Hwang, H. Tao, A. C. Strikwerda, K. Fan, G. R. Keiser, A. J. Sternbach, K. G. West, S. Kittiwatanakul, J. Lu, S. A. Wolf, F. G. Omenetto, X. Zhang, K. A. Nelson, and R. D. Averitt, Nature (London) **487**, 345 (2012).